Supporting Information for

Au–Ag Controllable Composition Nanoalloying of Hexagonal Nanoplates: Heterogeneous Interfacial Nanogap Enhances Near-Field Focusing

Sungbeen Park,[a] Insub Jung,[a] Soohyun Lee,[b] Qiang Zhao,[b] Sungwoo Lee,[b,c] Hyunji Kim,[a] and Sungho Park[a]*

[a]Department of Chemistry, Yonsei University, Seoul 03722, Republic of Korea

[b]Department of Chemistry, Sungkyunkwan University (SKKU), Suwon 16419, Republic of Korea

[c]Institute of Basic Science, Sungkyunkwan University (SKKU), Suwon 16419. Republic of Korea

*electronic mail: sparknano@yonsei.ac.kr

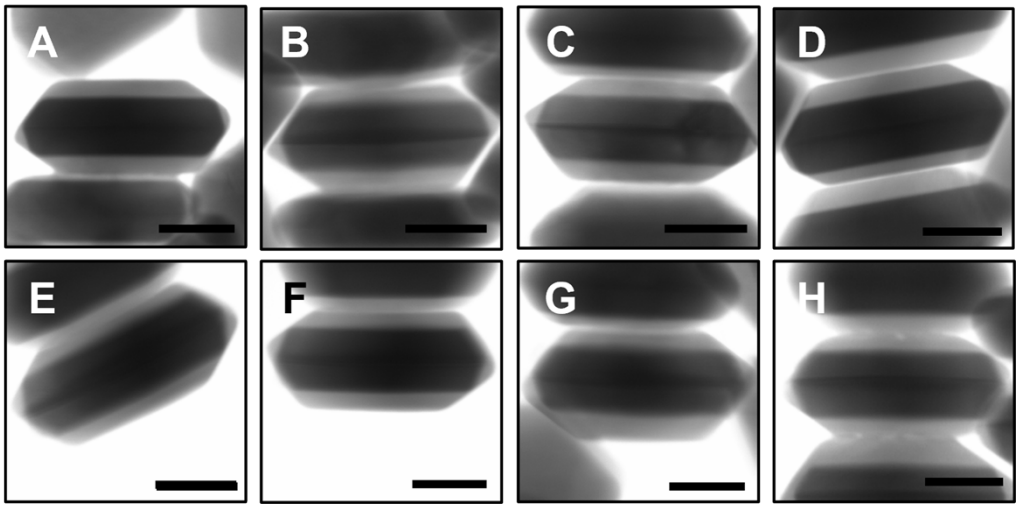

Figure S1. (A-H) Scanning transmission electron microscopy (STEM) images of Au@Ag h-NPLs over 8 samples captured in ⌙ bright field mode. All scale bars denote 50 nm.

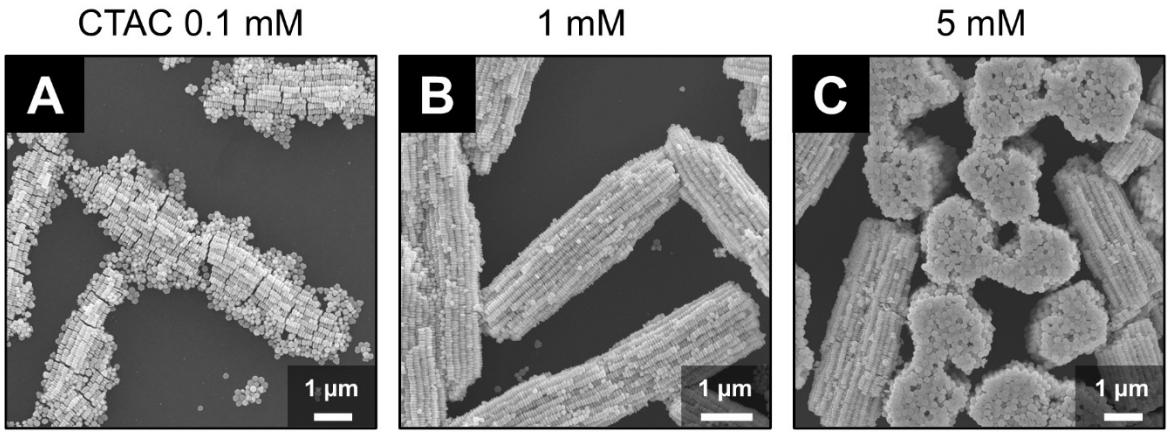

Figure S2. FE-SEM images of Au@Ag h-NPL assemblies synthesized under varying CTAC concentrations: **(A)** 0.1 mM, **(B)** 1 mM, and **(C)** 5 mM.

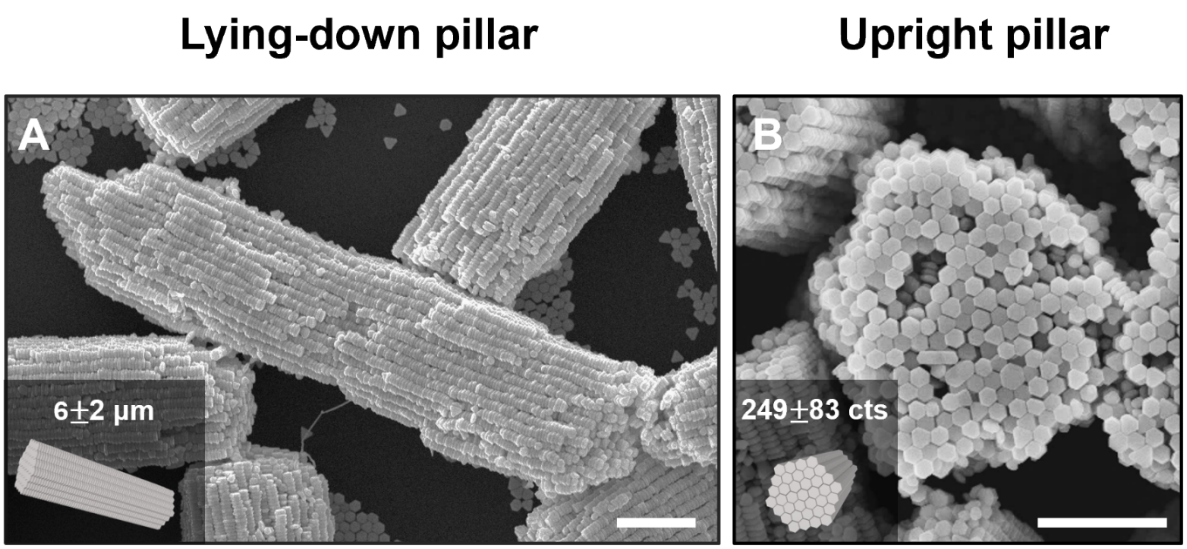

C Chunk length	Thickness of single particle	Number of upright-aligned particles	Total number of particles (single chunk)
6±2 μm	54±5 nm	249±83 cts	27666

Figure S3. FE-SEM images of the Au@Ag h-NPLs assembly; **(A)** Lying-down chunk, **(B)** Upright chunk. **(C)** Table used to estimate the total number of nanoparticles present in a single chunk. The total particle number per chunk was estimated by the formula: (chunk length ÷ thickness of a single particle) × number of upright-aligned particles. Scale bars denote 500 nm.

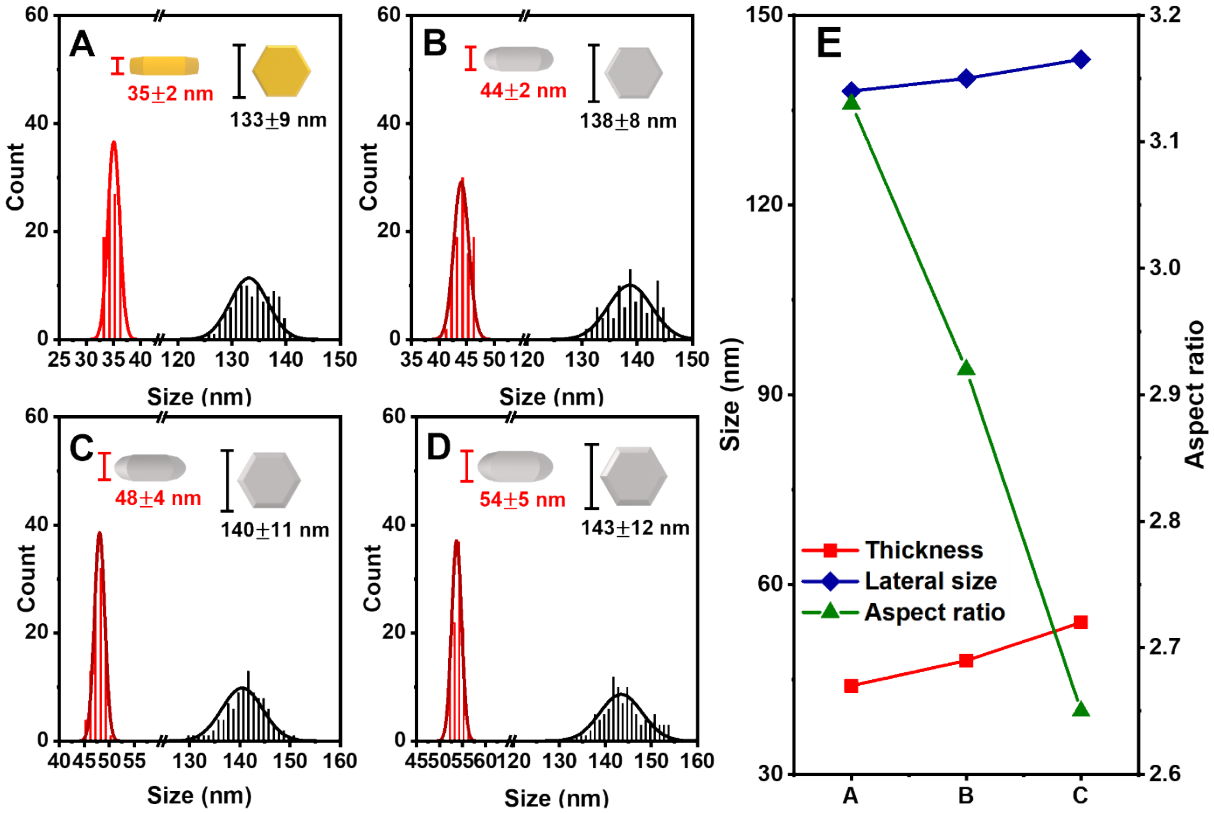

Figure S4. (A–D) Size distribution of Au h-NPLs and Au@Ag h-NPLs. **(E)** Line plot showing the aspect ratio of Au and Au@Ag h-NPLs as a function of Ag shell thickness.

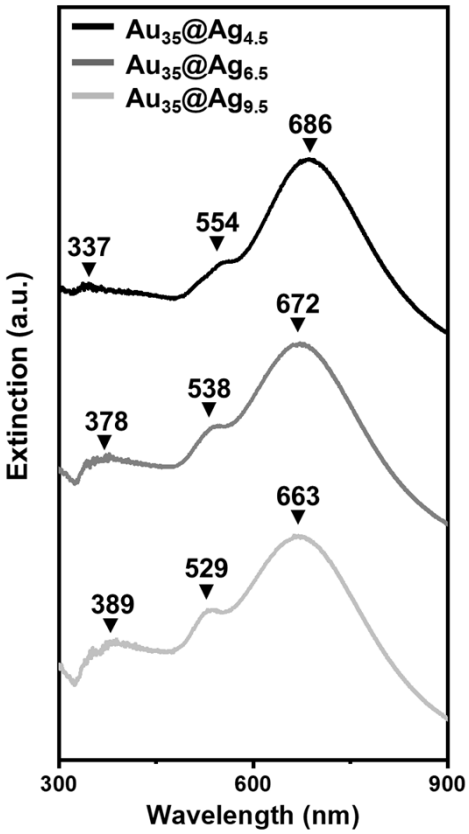

Figure S5. UV-vis-NIR spectra of Au@Ag h-NPLs with Ag shell thicknesses of 4.5 nm, 6.5 nm, and 9.5 nm.

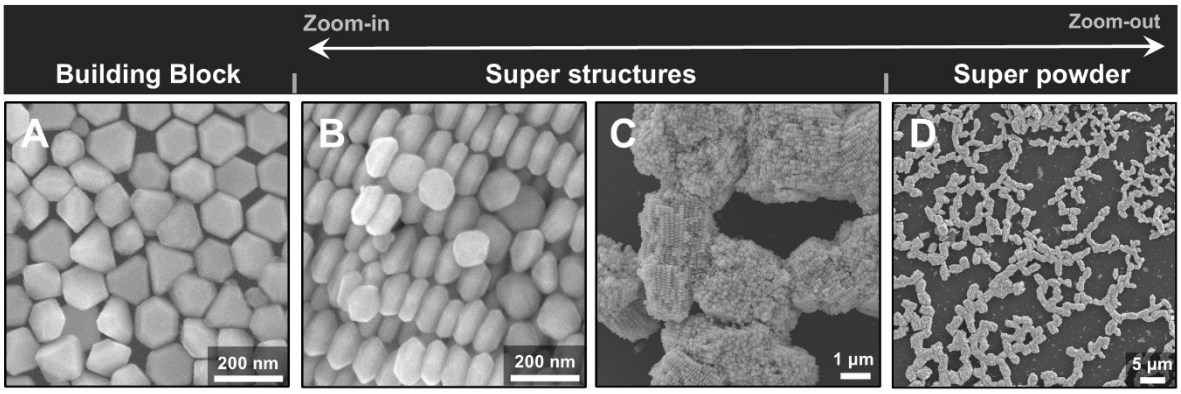

Figure S6. Formation of SPs from Au@Ag h-NPLs grown with an excess amount of Ag precursors.

Au	$Au_{35}@Ag_{4.5}$	$Au_{35}@Ag_{6.5}$	$Au_{35}@Ag_{9.5}$
31.57%	16.10%	3.29%	19.50%

Figure S7. RSD data of Figure 4E.

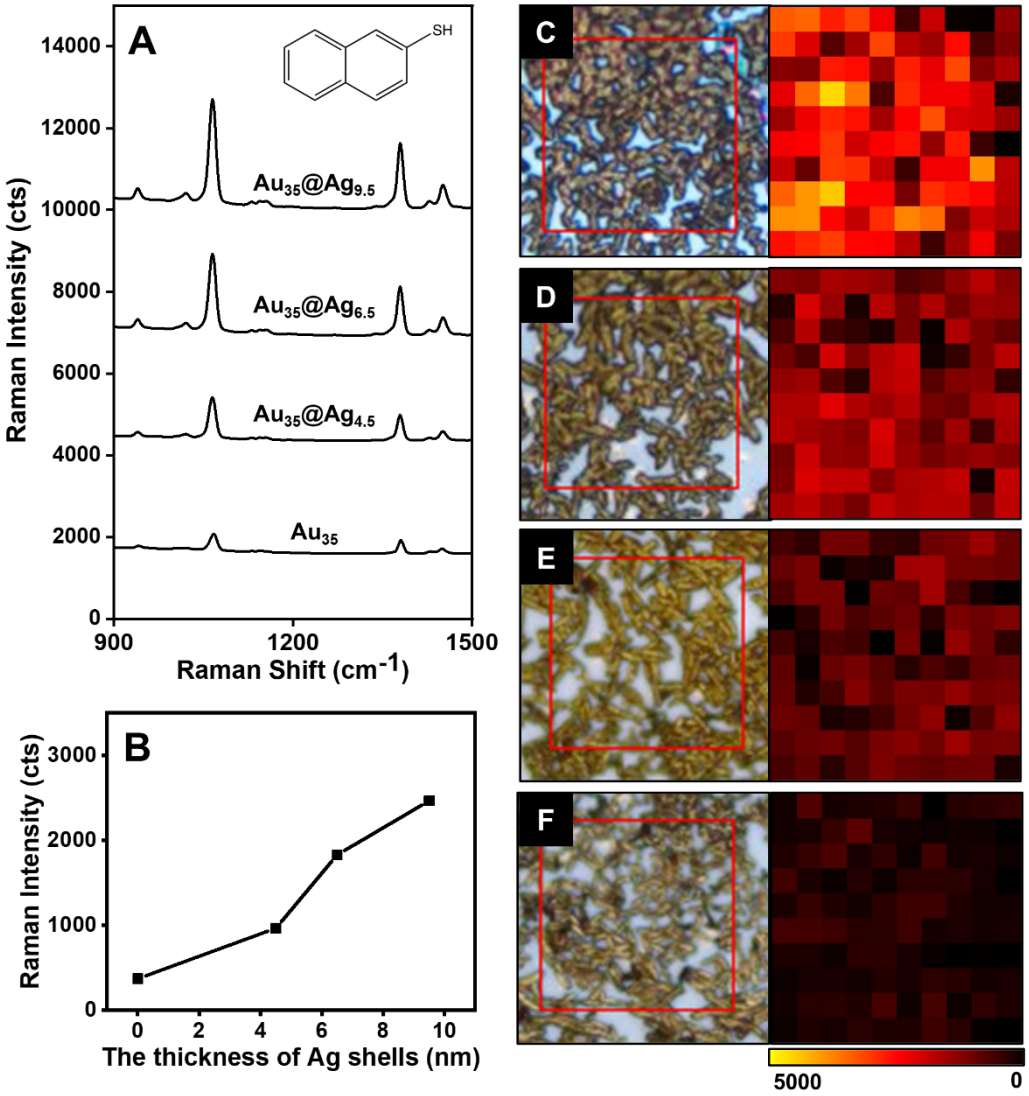

Figure S8. (A) SERS spectra of SPs composed of Ag core-shell h-NPLs with varying Ag shell thicknesses. **(B)** Line plot of SERS intensity at 1065 cm^{-1} as a function of Ag shell thickness. **(C–F)** Optical microscopy images of the measured areas and corresponding SERS mapping images, where each pixel represents 5 μm.

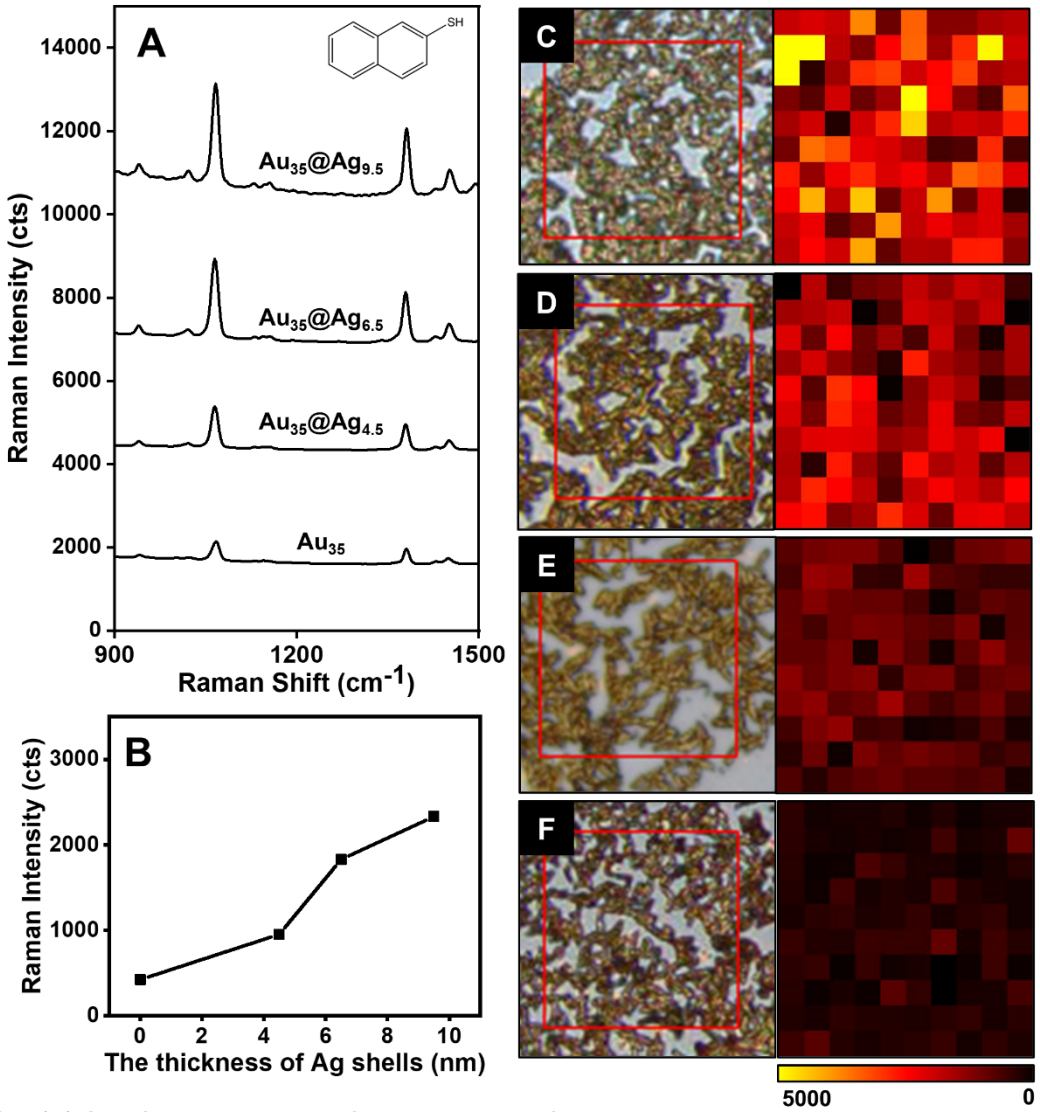

Figure S9. (A) SERS spectra of SPs composed of Ag core-shell h-NPLs with varying Ag shell thicknesses. (**B**) Line plot of SERS intensity at 1065 cm^{-1} as a function of Ag shell thickness. (**C–F)** Optical microscopy images of the measured areas and corresponding SERS mapping images, where each pixel represents 5 μm.

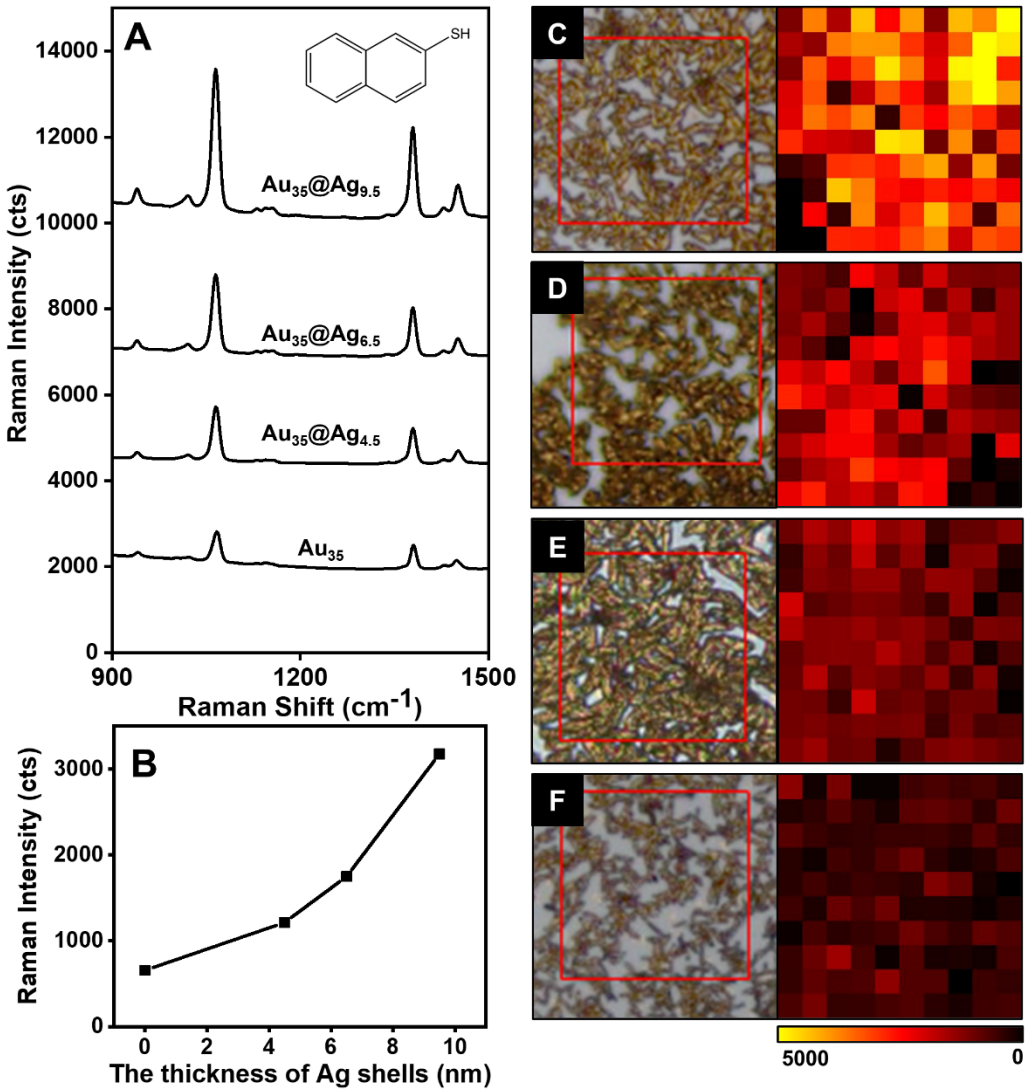

Figure S10. (A) SERS spectra of SPs composed of Ag core-shell h-NPLs with varying Ag shell thicknesses. **(B)** Line plot of SERS intensity at 1065 cm^{-1} as a function of Ag shell thickness. **(C–F)** Optical microscopy images of the measured areas and corresponding SERS mapping images, where each pixel represents 5 μm.

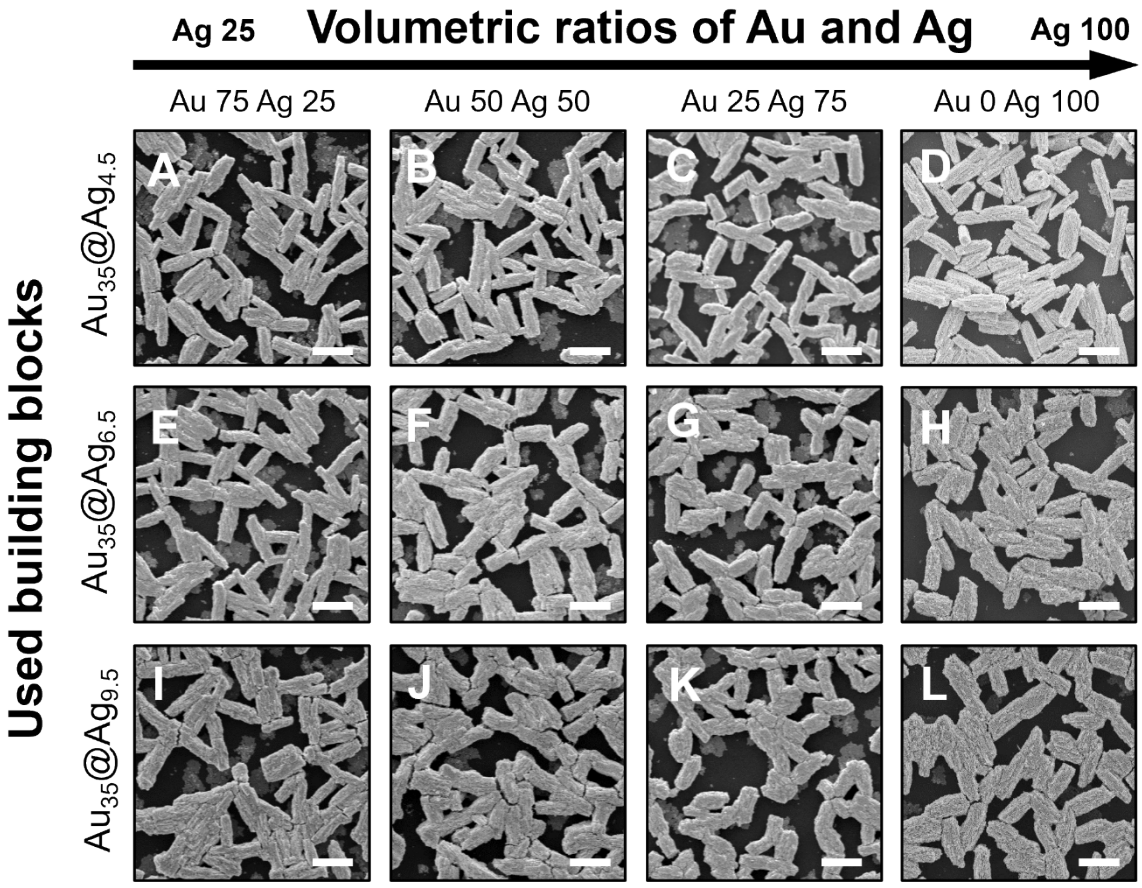

Figure S11. SPs formed by combining Au@Ag h-NPLs of varying Ag shell thicknesses with Au h-NPLs at different ratios. Scale bars represent 1 μm.

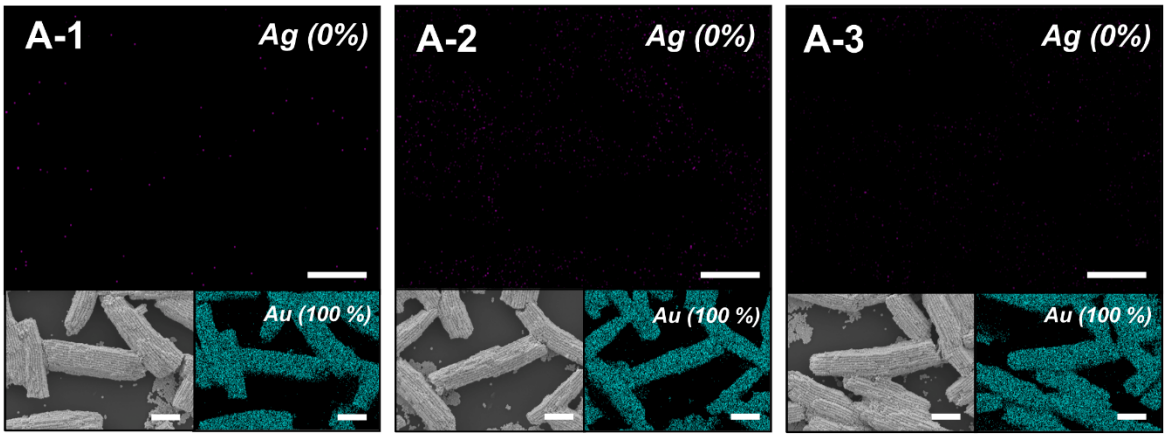

Figure S12. FE-SEM and EDS mapping images of SPs composed entirely of pure Au h-NPLs. Scale bars represent 2 μm.

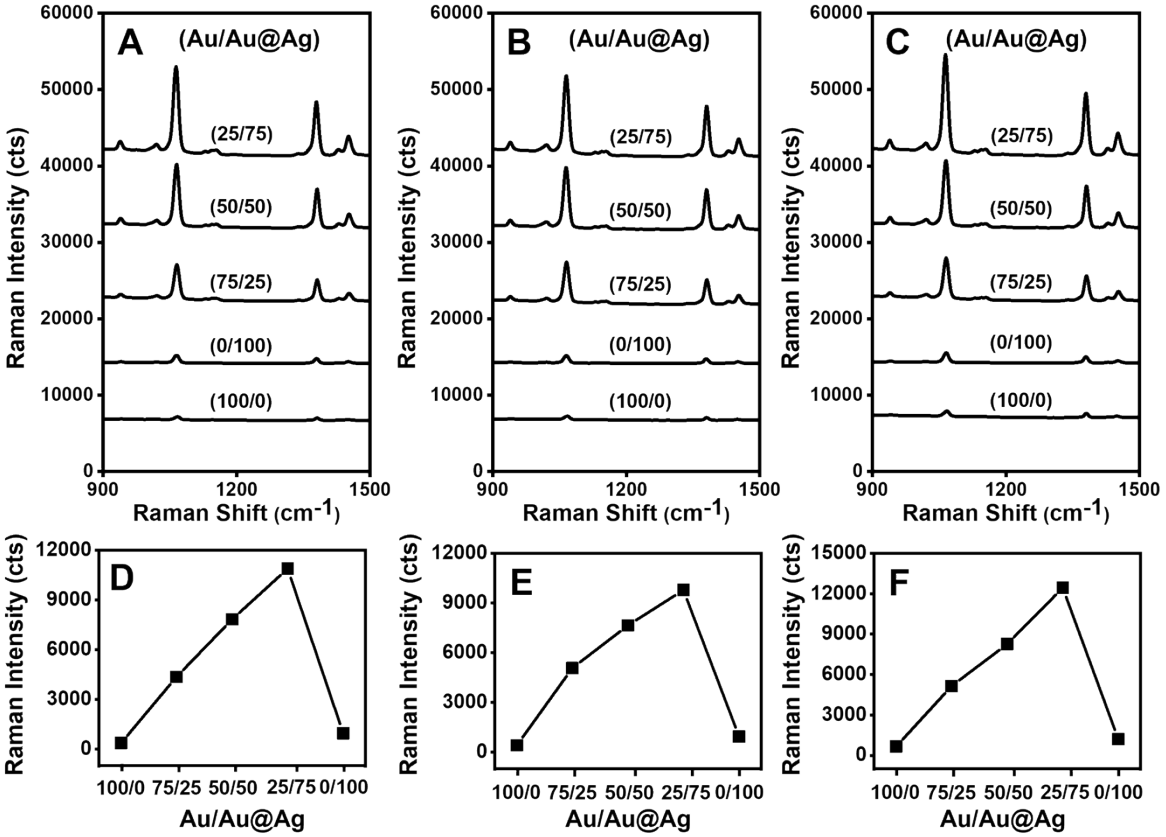

Figure S13. (A–C) SERS spectra for SPs formed from varying ratios of Au h-NPLs and $Au_{35}@Ag_{4.5}$ core-shell h-NPLs. **(D–F)** Line plots of SERS intensity at 1065 cm^{-1} as a function of the Au-to-Au@Ag h-NPL ratio.

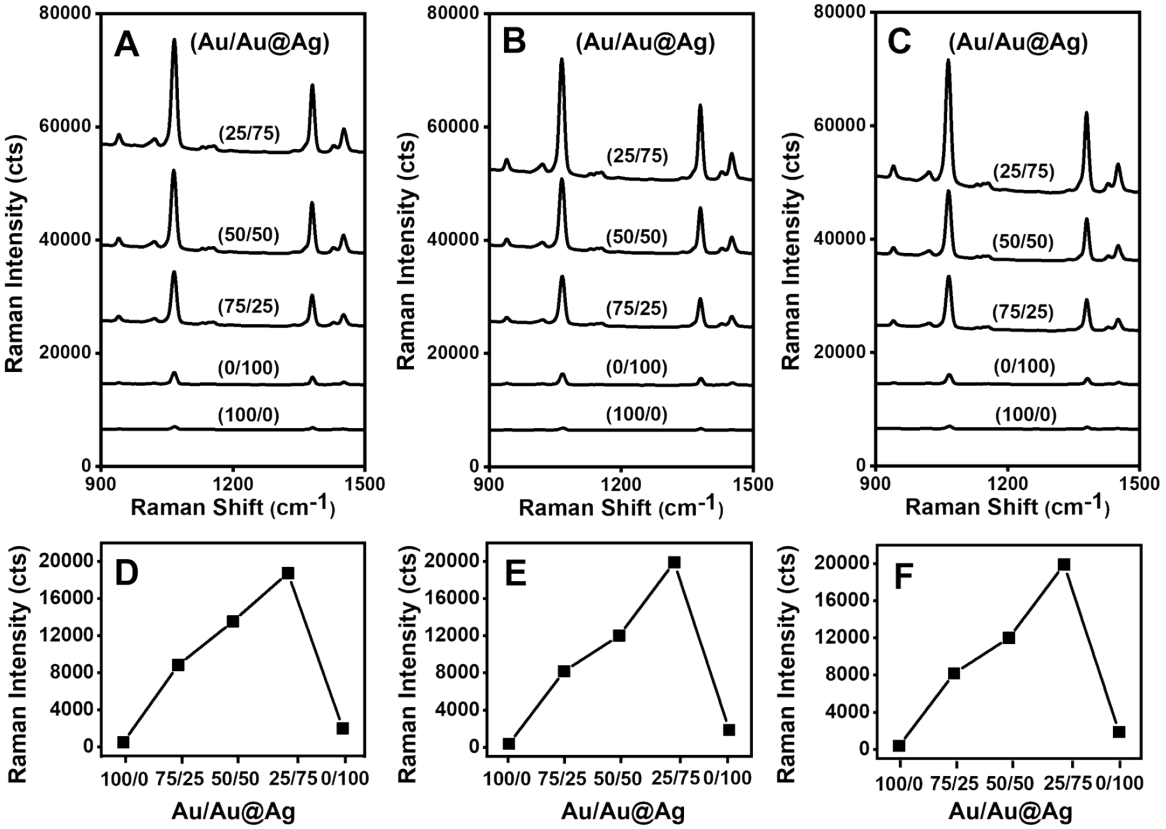

Figure S14. (A–C) SERS spectra for SPs formed from varying ratios of Au h-NPLs and $Au_{35}@Ag_{6.5}$ core-shell h-NPLs. **(D–F)** Line plots of SERS intensity at 1065 cm^{-1} as a function of the Au-to-Au@Ag h-NPL ratio.

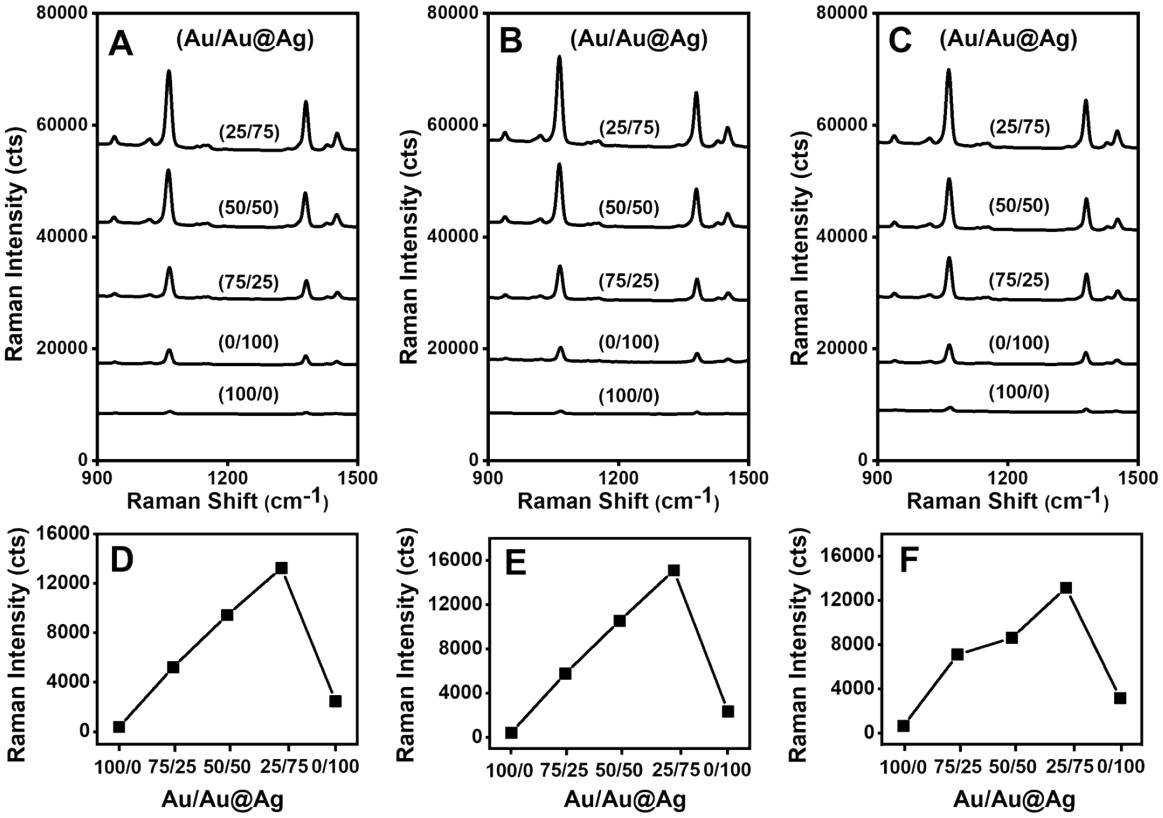

Figure S15. (A–C) SERS spectra for SPs formed from varying ratios of Au h-NPLs and $Au_{35}@Ag_{9.5}$ core-shell h-NPLs. **(D–F)** Line plots of SERS intensity at 1065 cm^{-1} as a function of the Au-to-Au@Ag h-NPL ratio.

	100/0	75/25	50/50	25/75	0/100
$Au_{35}@Ag_{4.5}$	16.34%	5.87%	4.27%	12.72%	16.01%
$Au_{35}@Ag_{6.5}$	16.34%	4.92%	10.56%	6.25%	9.72%
$Au_{35}@Ag_{9.5}$	16.34%	17.94%	7.79%	9.17%	19.50%

Figure S16. RSD data of Figure 6D.

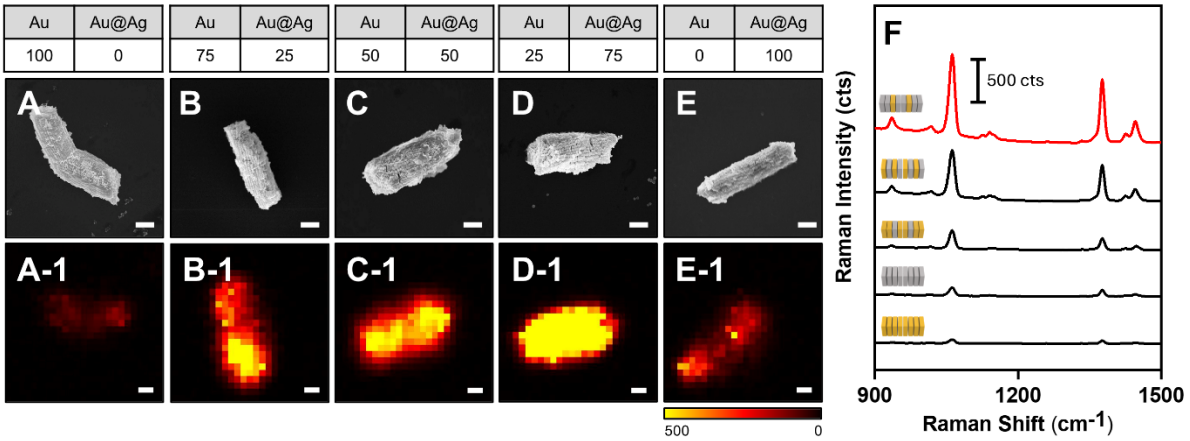

Figure S17. FE-SEM and mapping images of single chunks of SPs consisting of **(A)** pure Au h-NPLs superstructures, **(B–D)** Au–Au@Ag binary h-NPL superstructures with varying volumetric ratios, and **(E)** pure Ag h-NPLs superstructures. Scale bars in panels **(A–E)** represent 1 μm. **(F)** SERS spectra of 2-NTT (10^{-2} M) for Au–Au@Ag binary h-NPL superstructures at varying ratios under 785 nm excitation. The red spectrum corresponds to the superstructure with an Au:Au@Ag ratio of 1:3, which exhibits the strongest SERS signal among the investigated single chunks of SPs.

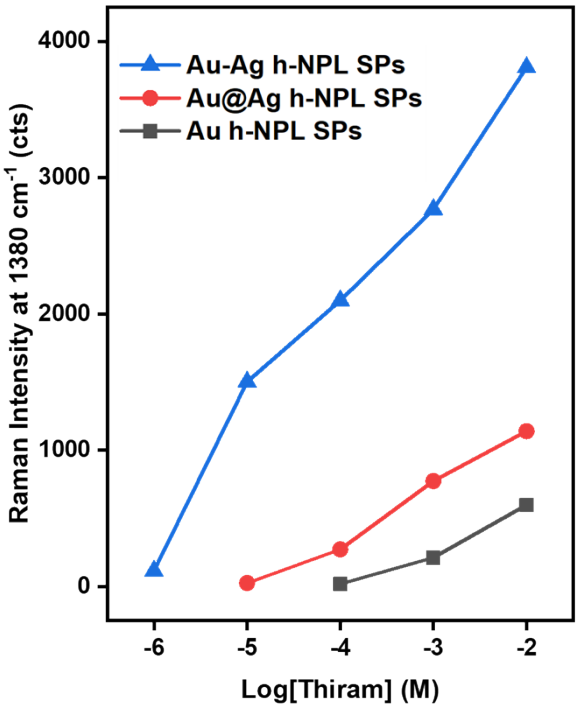

Figure S18. Calibration curves of SERS intensity Thiram using heterogeneous Au-Ag h-NPL SPs (blue line), Au@Ag h-NPL SPs (red line) and Au h-NPL SPs (black line).

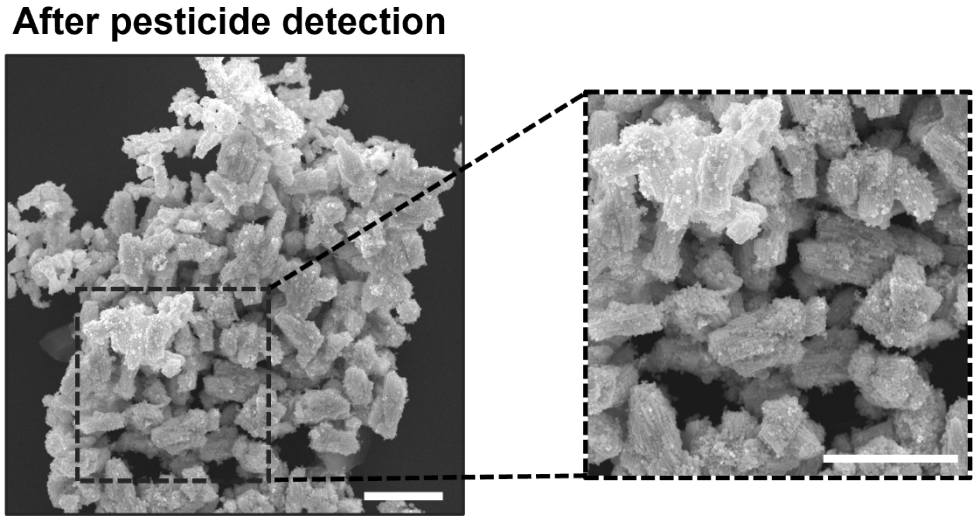

Figure S19. FE-SEM image of SP consisting of Au-Au@Ag h-NPLs after detecting pesticide. Scale bars denote 5 μm.